IEEE Access
Multidisciplinary | Rapid Review | Open Access Journal

Received 1 July 2023, accepted 16 July 2023, date of publication 24 July 2023, date of current version 1 August 2023.

Digital Object Identifier 10.1109/ACCESS.2023.3298298

RESEARCH ARTICLE

Switchable THz Guided Mode Enhancement in Subwavelength Thick PTFE – Polyimide Based Metamaterial Devices

S. M. RAKIBUL HASAN SHAWON, (Student Member, IEEE), SAJIB KAPALI, IMI BINTEY FARIHA RAHMAN, (Student Member, IEEE), SHARNALI ISLAM, AND KHALEDA ALI

Department of Electrical and Electronic Engineering, University of Dhaka, Dhaka 1000, Bangladesh

Corresponding author: Khaleda Ali (khaleda.eee@du.ac.bd)

This work was supported by the Centennial Research Grant (Second Phase), University of Dhaka.

ABSTRACT We report an efficient approach to enhance terahertz (THz)-guided modes for realizing subwavelength thick metamaterial devices (MMD). Here, a combination of hollow and slitted rings of the vanadium dioxide (VO_2)-based metasurface, having perfect impedance matching with free space, is considered to cause tight coupling in the unit cells while reducing transverse field components of the boundary. The consolidated dielectric layer of polytetrafluoroethylene (PTFE)-polyimide underneath, maintaining a gradual change in refractive indices, brings about further improvement for a broader spectrum. Through strategic and systematic design steps, a maximum impedance bandwidth of 5.68 THz, ranging from 4.42 to 10.10 THz, has been achieved here from a structure thinner than a wavelength. Additionally, mode-independent polarization insensitivity and tunability are attained through the symmetrical unit cell pattern of temperature-dependent VO_2. Optimized design parameters agree with interference cancellation theory too. Validation of our presented design is performed using theoretical analysis based on equivalent circuit theory. The proposed design offers a new avenue for designing ultra-thin broadband absorbers, light modulators, etc.

INDEX TERMS Absorber, metamaterial devices, metasurface, light modulator, THz guided mode enhancement.

I. INTRODUCTION

Artificially engineered electromagnetic (EM) materials having subwavelength structural details possess unique attributes. Design flexibility offered by these metamaterials aids in realizing devices for a plethora of applications, including elimination of undesired EM energy interference, stealth technology [1], sensing [2], [3], photovoltaics [4], imaging [5], medical applications [6], etc. Owing to the negative refractive indices of these novel constituents, metasurfaces allow sleeker and lighter designs compared to conventional structures performing similar functions [7], [8]. Most of these application areas, however, necessitate metamaterials to enhance surface current at the interface and result in devices with near-unity absorption at the designated spectrum.

Recent evidences suggest considerable progress in the advancement of metamaterial based devices (MMD) [9], [10], [11], [12], [13], [14]. Work in [12] reports a rotationally symmetric patch integrated layout to strengthen surface current at the Ku band. For near-infrared (NIR) range, gallium-doped zinc oxide-based nanorods ensuring high absorption have been incorporated [14]. A detailed analysis on the device's performance for varying incident angles and nanorod volume fractions has also been addressed. Falling between the gigahertz (GHz) and optical spectra that are governed by classical electron transfer theory and quantum mechanics, respectively, a comparatively less exploited spectrum remains, broadly known as the terahertz (THz) gap.

The associate editor coordinating the review of this manuscript and approving it for publication was Lei Zhao.

Such spectrum (0.1-11 THz) is significant for the advancement of the sixth-generation (6G) THz wireless networks [15], imaging technology [16], particularly in manipulating THz radiation [17], generation [18], and detection [19], [20], spectroscopy, quantum electronics, etc [21], [22], [23], [24].

To trap THz waves in a narrow and broad band, a list of suitable conducting and dielectric materials for THz devices is presented in [22]. Studies on architectural changes, including circular and square rings [25], [26], wheel patterns [27], multi-layered metals of pyramidal shape [28], and all-dielectric-based layouts [29], have also been demonstrated. However, these top conducting planes primarily leverage to narrow band response. Frequency-dependent molecular absorption is also a factor behind limiting absorption bandwidths. Multi-layered conductors with dielectric spacers or graphene-incorporated hybrid metasurfaces, enhancing guided wave for larger bandwidth has been reported in [30], [31]. Nonetheless, the achieved unit cells require a thicker dielectric layer to reduce backward transmission, and double-layer conductor deposition, which substantially increases fabrication complexity. It is worth mentioning that the available literature mostly leads to their proposed solution through the trial and error method, rather than strategic design steps. Existing literature also demonstrates the inclusion of active photonic materials [32], [33], [34], [35] that are able to actively control and manipulate the absorption properties. In [32], however, it is observed that while silicon acts as an insulator, the cross-polarized reflected wave increases with a reduction in the guided wave. Similar scenario is apparent in [33] with vanadium dioxide (VO_2). On the other hand, the incorporation of active photonic materials as either a metal or an insulator, while simultaneously maintaining minimized reflection, greatly facilitates the development of devices capable of modulation, switching, or tunable filtering. To this aim, our work focuses on achieving a tunable, ultrawideband, polarization-insensitive device by enhancing guided waves at the conducting plane in a systematic manner. Here, guided mode indicates the transmission modes with complex wavenumbers, tightly coupled to the metal-dielectric interface. As a metasurface, we propose a VO_2 based arrangement of rings onto which multiple slits are strategically etched. Each of the rings has separate narrow yet closely spaced impedance bandwidths that are leveraged to improve the total bandwidth of the guided wave. Below the conductive layer, two different dielectric spacers with increasing dielectric constants are placed to direct and trap the wave inside this cavity within a smaller distance. From the optimized design, a bandwidth of 5.68 THz is achieved, and to the best of the author's knowledge, this is the highest bandwidth reported in the literature, from a subwavelength thick broadband THz device. Validation of the result in terms of equivalent circuit theory has also been showcased in this work. The analysis is conducted within the 1-11 THz range to enable the effective use of our proposed MMD in high-speed data transmission and applications requiring precise frequency control. Since the proposed outcome of $\lambda/3$ thickness can easily be adopted as a metamaterial absorber (MMA) and light modulator, therefore all the analyses in the rest of the sections have been made focusing on these two applications.

II. DESIGN

The proposed optimized ultra-wideband thin THz MMD is presented in Fig. 1. Here, the unit cell is represented by a VO_2 coated dual layered dielectric substrate of PTFE-polyimide combination covering an area of $40 \times 40\ \mu m^2$. The dielectric properties of these two sheets are provided in Table 1.

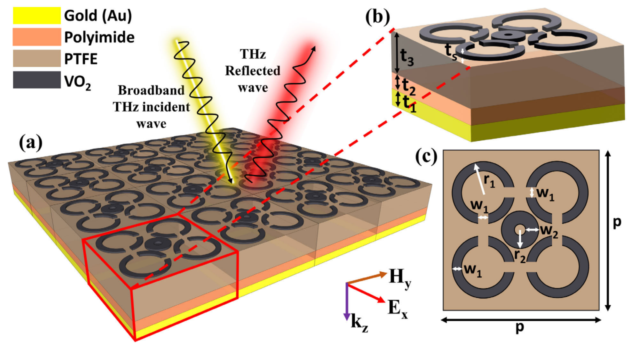

FIGURE 1. Schematic Illustration of the proposed THz device identifying (a) three dimensional (3D) periodic array, (b) isometric view of the unit cell with structural parameters, and (c) the top view of the unit cell with period p = 40 μm.

TABLE 1. Properties of the dielectric layers.

Material	PTFE	Polyimide
Relative Permittivity	$\varepsilon_{rPTFE} = 2.1$	$\varepsilon_{rPO} = 3.5$
Loss tangent ($tan\delta$)	0.0002	0.0027
Thickness (μm)	4.8	1.9

Thicknesses of PTFE (t_3) and polyimide (t_2) are kept as $0.01 \times \lambda_{min}$ and $0.03 \times \lambda_{min}$ respectively, where λ_{min} indicates minimum wavelength in respective media. Hence the effective dielectric constant (ε_{effD}) of the dual-layered part can be presented as in (1) [36]:

$$\varepsilon_{effD} = \frac{\varepsilon_{rPTFE} + \varepsilon_{rPO} + (\varepsilon_{rPO} - \varepsilon_{rPTFE}) \cos \frac{\pi t_3}{t_2 + t_3}}{2} \tag{1}$$

The dielectric properties of VO_2 in the THz range have been extracted following Drude model [37], [38] (see, Fig. 2(a)-(c)), where permittivity (ε) at angular frequency (ω) can be expressed as:

$$\varepsilon(\omega) = \varepsilon_\infty - \frac{\omega_p^2(\sigma)}{\omega^2 + i\gamma\omega} \tag{2}$$

Here, dielectric permittivity at infinite frequency (ε_∞) and the collision frequency (γ) are set to 12 and 5.75×10^{13} rad/s respectively. For two different conductivity of σ and σ_0, plasma frequency (ω_p) can be represented as:

$$\omega_p^2(\sigma) = \frac{\sigma}{\sigma_0}\omega_p^2(\sigma_0) \tag{3}$$

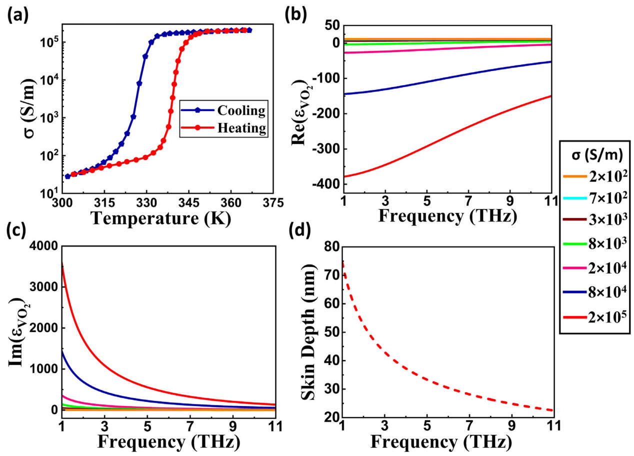

FIGURE 2. ***VO_2*'s (a) temperature dependant conductivity, (b) real and (c) imaginary parts of permittivity, and (d) variation of skin depth of gold with frequency.**

with $\sigma_0 = 3.0 \times 10^5$ S/m and $\omega_p(\sigma_0) = 1.4 \times 10^{15}$ rad/s. Under various temperature conditions, the effective conductivity of VO_2 can be expressed as [39]:

$$\sigma = \sigma_{eff_{VO_2}}(T) = -i\epsilon_0\omega\left[\epsilon_{eff_{VO_2}}(T) - 1\right] \tag{4}$$

It is worth mentioning that from 300K to 350K, the conductivity (σ) of VO_2 may vary from 25 S/m to 2×10^5 S/m as it undergoes a phase transition from insulator to metal state (ITM) at 340K (see, Fig. 2(a)) [40]. Hence, the Bruggeman effective-medium theory (BEMT) can be used to explain the complex dielectric properties of VO_2 as follows [41]:

$$\epsilon_{eff_{VO_2}}(T) = \frac{1}{4}\left[\epsilon_i(2-3V_f) + \epsilon_m(3V_f-1)\right] + \frac{1}{4}\left[\sqrt{[\epsilon_i(2-3V_f) + \epsilon_m(3V_f-1)]^2 + 8\epsilon_i\epsilon_m}\right] \tag{5}$$

where the corresponding dielectric permittivity of VO_2's insulating and metallic phases are defined as ϵ_i and ϵ_m. Additionally, by using the Boltzmann distribution function, the fractional volume of the metallic region, V_f can be represented as:

$$V_f = V_f(T) = V_{max}\left[1 - \frac{1}{1 + e^{\frac{T-T_c}{\Delta T}}}\right] \tag{6}$$

where $T_c = 68$ °C implies the critical temperature for phase change in the heating process, and ΔT = 2 °C indicates the deviation of temperature due to external thermal energy from heating to cooling operation; the largest volume distribution in the metallic form during the phase transition is V_{max} ($\approx$0.95) [42].

To determine the permittivity of VO_2 using BEMT, it is required to ensure that the size of the VO_2 layer remains smaller than the operating wavelength. However, it still needs to be of sufficient magnitude to be described by a dielectric function. This is essential since for a fractional volume (V_f) over 20%, the interaction among the random yet macroscopically homogeneous metallic particles in the insulating phase of VO_2 can no longer be ignored.

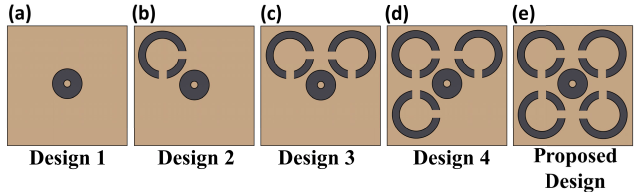

FIGURE 3. Design hierarchy of unit cell of MMD consisting of (a) a central ring resonator, (b) one, (c) two, (d) three, and (e) four double slitted rings with central ring.

TABLE 2. Ring Resonators parameter list.

Parameters	r_1	w_1	r_2	w_2
Values (μm)	9	2	4.5	3.5

The proposed design is achieved through strategic steps for enhancing the resonant mode of surface waves as shown in Fig. 3 (a) - (e). In design 1, a single VO_2 ring (outer radius, $r_o = 4.5$ μm) is considered for the simulation with a periodicity of $p = 40$ μm. To strengthen the surface wave, double slitted ring is added in design 2 (as in Fig. 3(b)). The goal is to capture and focus the incident wave near the periphery of the central ring. To this aim, one ring in each design step has been added sequentially; orthogonal slits are etched, making the slits of adjacent rings in line of sight. The thickness of these double slitted rings is kept at 0.2 μm with gaps of 2 μm length. Dimensions of the rest of the parameters are provided in Table 2.

The radius, width, and split gaps of different rings are altered since these parameters influence the enhancement of surface wave propagation. Double-layered dielectric surfaces (PTFE and polyimide) backed by a gold (Au) layer have been incorporated in this study, causing a reduction of reflected fields. Such composition aids to achieve 90% absorption. Since polytetrafluoroethylene (PTFE) is optically lighter compared to polyimide in terms of reflection coefficient; therefore, it is placed adjacent to VO_2. At the bottom of the structure, 2 μm thick Au with an electrical conductivity of 4.56×10^7 (S/m) is placed. The height of the ground is usually kept higher than its skin depth to restrict the transmitting field (see, Fig. 2(d)).

The numerical investigation has been carried out using a frequency domain solver of the commercial software CST Microwave Studio. In the simulation domain, Maxwell's equations are solved by considering a unit cell with periodic boundary conditions along the x and y directions. Scattering parameters have been calculated using a broadband EM source spanning from 1-11 THz applied via floquet ports oriented along the z axis.

A possible setup for constructing the optimized MMD, is presented in Fig. 4. Here, for the fabrication of the unit cell, initially, a polyimide film of thickness 1.9 μm is aimed to be

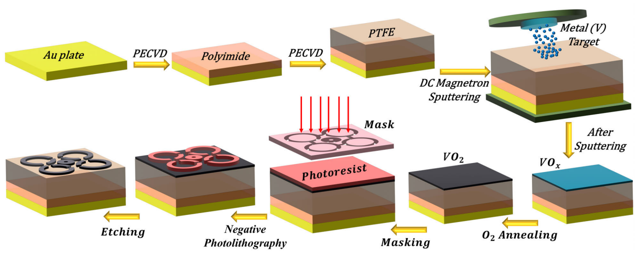

FIGURE 4. Fabrication steps of the unit cell of the MMD.

deposited onto a 2 μm thick Au plate by plasma enhanced chemical vapor deposition (PECVD) process. The PTFE layer would later be coated by applying the same method. VO_2 film can be grown onto PTFE using dc magnetron sputtering, in a vacuum chamber, with a vanadium metal target as the cathode. For this, at first, PTFE is coated with VO_x after it has been sputtered, and then is subsequently annealed in a low-pressure oxygen (O_2) environment to change the VO_x into VO_2 [43]. A surface pattern mask, following a photoresist, is deposited and through negative photo-lithography, the optimized pattern of photoresist is obtained. Finally, the etching process brings out the desired outcome. To adjust tunability, the temperature of the MMD can be elevated using a resistive heater positioned underneath the gold plate. In addition to thermal excitation, the characteristics of VO_2 can be modified through electrical [44] and optical [45] stimulation also.

III. RESULT ANALYSIS

The absorption spectra of the presented designs (as in Fig. 3(a) -(e)) are estimated using (7) [33]:

$$A(\omega) = 1 - R(\omega) - T(\omega) - P(\omega) \tag{7}$$

Here, R(ω) and T(ω) represent the reflection and transmission coefficient respectively at angular frequency (ω), which in terms of scattering parameters can also be denoted as $R(\omega) = |S_{11}|^2$ and $T(\omega) = |S_{21}|^2$. The polarization conversion, $P(\omega)$, is allowed to be close to zero due to the resonant unit structure configuration of the MMD. Since no EM wave is transmitted through the absorber, the transmittance T(ω) can be omitted from (7), and the absorptance can be mentioned as:

$$A(\omega) = 1 - |S_{11}(\omega)|^2 \tag{8}$$

Based on (8), the absorptance of different resonating structures is estimated and presented in Fig. 5(a). Here, for design 1 (see, Fig. 3(a)), multiple picks are observed in the green curve (see, Fig. 5(a)). It occurs since the $\frac{r_0}{p}$ influences resonance; the higher the ratio $\frac{r_0}{p}$, the higher is the number of resonating vertices in the absorption spectra. Later, upon adding each double slitted rings, bandwidths expand. The series inductances for double slitted ring, mutual inductances between rings, gap capacitances, and capacitances among rings all aid in enhancing absorption at the broader spectrum. For the dielectric, the gradual change in refractive indices

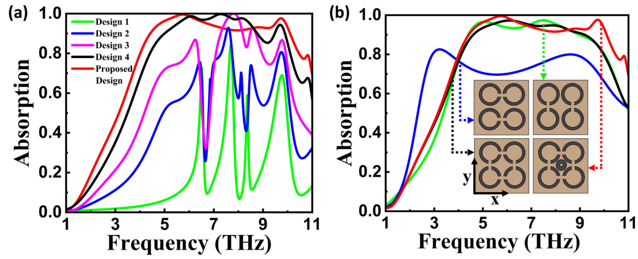

FIGURE 5. Absorption spectrum (a) for design 1 - proposed design, and (b) for varying slit positions in multi-ring based MMDs.

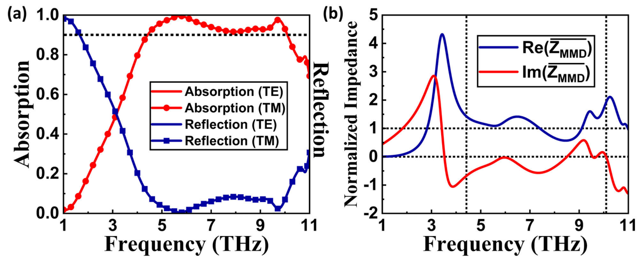

FIGURE 6. (a) The reflection and absorption spectrum, and (b) components of complex normalized impedance of MMD.

tends to impede reflection at the interfaces and essentially results in a comparatively thinner metamaterial absorber. For normal incidence of EM wave, the final design of Fig. 3(e) has the highest absorption bandwidth of 5.68 THz spanning from 4.42 THz and 10.10 THz, as provided in Fig. 6(a). The central frequency between the two absorption peaks is 7.735 THz, and the relative absorption bandwidth (RABW) $\frac{2(f_{MAX}-f_{MIN})}{f_{MAX}+f_{MIN}}$ [46] is 78.24%, where f_{MAX} and f_{MIN} represent the maximum and minimum frequencies with greater than 90% absorption, respectively. Hence, the recommended outcome tends to offer ultra-wideband performance. Three different arrangements of surrounding rings have also been presented in Fig. 5(b). However, the double slits near the central ring in the proposed design (see, Fig. 3(e)) significantly contribute to the capacitance on the front plane and ensure a tight coupling of surface current at the VO_2 - air interface.

The appropriateness of our design parameters has also been claimed by implementing the impedance matching theory to it [47]. To this aim, the complex impedance of the MMD (Z_{MMD}) is evaluated from the simulated scattering properties as:

$$Z_{MMD} = \pm\sqrt{\frac{(1+S_{11})^2 - {S_{21}}^2}{(1-S_{11})^2 - {S_{21}}^2}} \tag{9}$$

Having S_{21} equal to zero, in terms of normalized impedance $\overline{Z_{MMD}}$, S_{11} and A can be written as:

$$S_{11} = \frac{Z_{MMD} - Z_0}{Z_{MMD} + Z_0} = \frac{\overline{Z_{MMD}} - 1}{\overline{Z_{MMD}} + 1} \tag{10}$$

$$A = 1 - |S_{11}|^2 = \frac{4Re(\overline{Z_{MMD}})}{[Re(\overline{Z_{MMD}}) + 1]^2 + [Im(\overline{Z_{MMD}})]^2} \tag{11}$$

For capturing maximum power, our optimized double dielectric-based structure requires matching its impedance (Z_{MMD}) to that of the free space (Z_0). In line with this, for the proposed optimized design, Fig. 6 demonstrates that at frequencies showing maximum absorption (as in Fig. 6(a)), the real and imaginary components of normalized impedance values (see, Fig. 6(b)) are near unity and zero respectively. To be specific, at the peak absorption frequency, 5.74 THz, $\overline{Z_{MMD}} = 1$. It is worth noting that the electrical dimension of the height of the dual layer dielectric is 1/4 th of the central wavelength (in the dielectric layer) 25.35 μm, which meets the interference cancellation criteria between the reflected and incident waves and maintains impedance matching.

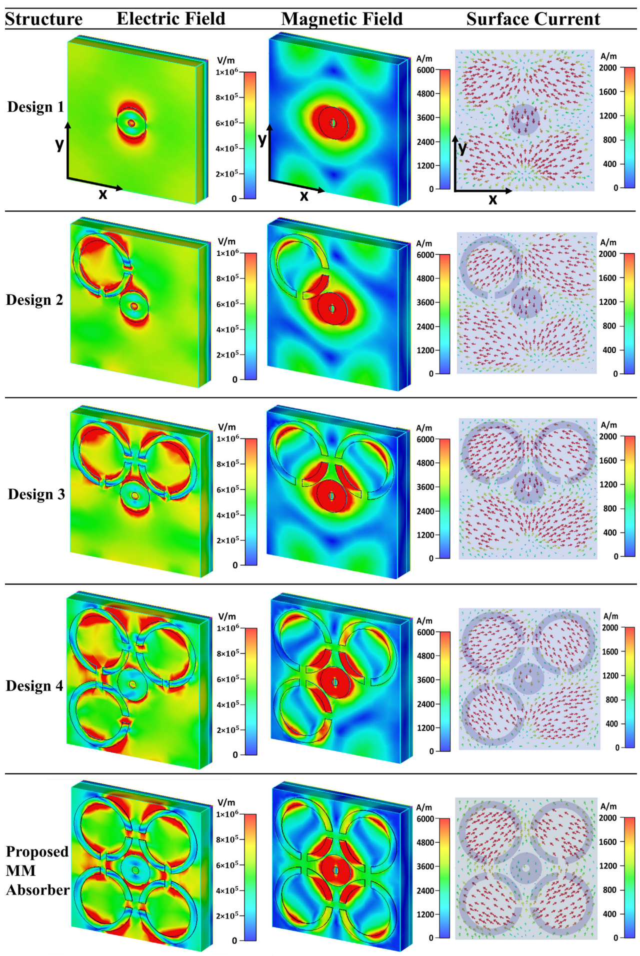

FIGURE 7. **Electric field, magnetic field and surface current distribution (bottom) at 9.73 THz for design1-proposed design.**

To gain a better understanding on the propagation phenomena, Fig. 7 further demonstrates the electric field, magnetic field, and surface current distributions for all the designs at 9.73 THz. The localization of the maximum electric field near the central ring is evident in Fig. 7 (Proposed MM Absorber), which points to ultrawideband performance.

For further validation of the broadband performance from the optimized layout, the electric field on the top surface and surface current distribution at the bottom polyimide-Au interface are presented in Fig. 8. At 6.73 THz, the electric field is mainly concentrated around the central hollow rings and in the inter-ring gaps. In such a scenario, certain positive charges can be equally arranged at the locations (marked by "O") where strong electric fields are imminent. Similarly, surface currents, oriented along the -y direction and centered upon the upper and lower parts of the peripheral rings act as negative charges on the Au layer. Hence, the top and bottom conducting surfaces form an electric dipole while EM wave penetrates through the structure. This in turn initiates magnetic resonance and enables the device to act as an absorber.

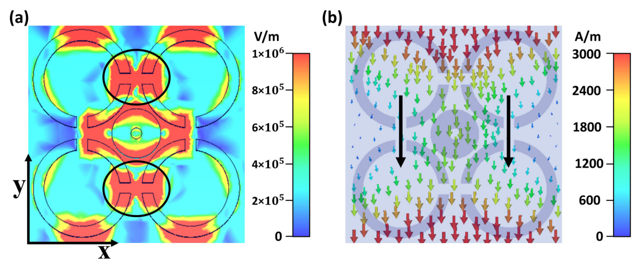

FIGURE 8. **(a) E field, and (b) surface current distribution at 6.76 THz.**

To investigate polarization dependency, the proposed optimized MMD is illuminated with a THz source of different polarization angles ranging from 0° to 90°. Having a symmetrical configuration, our design manifests itself as polarization insensitive for both transverse electric (TE) and transverse magnetic (TM) modes (see, Fig. 9).

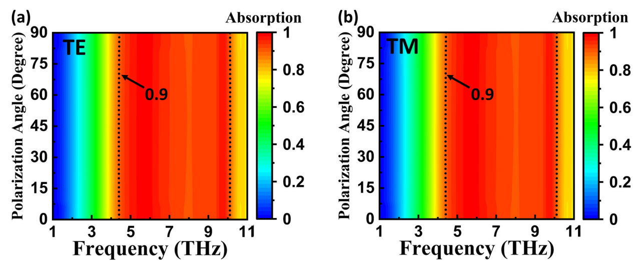

FIGURE 9. **The absorption spectra under different polarization angles for (a) TE, and (b) TM polarization.**

Effects of incident angle variations have also been taken into account (see, Fig. 10). Here, the incident angles

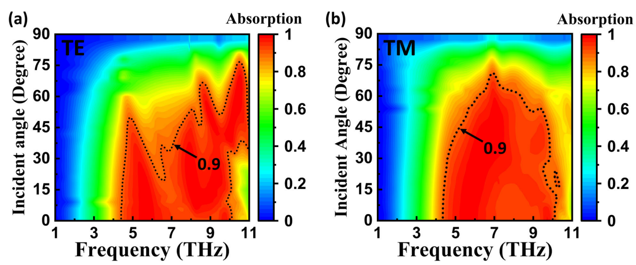

FIGURE 10. **The absorption spectra under different incident angles for (a) TE, and (b) TM polarization.**

incrementally adjusted in a step of 3° from 0° to 90° cause stable output till 56° and 64° for TE and TM polarization, respectively. Increased obliquity results in decreased absorption.

As a closer view, Fig. 11 reports the response of MMD at two distinct frequencies for two different polarizations. It is observed that at 5.5 THz for TE polarization, over 40.6° absorption reduces to 0.9, and for TM polarization at 6.93 THz, similar things happens at 73.5°. Here, an increase in the incidence angles results in longer path lengths, and hence the coupling effect gets lowered. This further reduces dipolar resonance and electromagnetic wave confinement within the dielectric layer. Nevertheless, the absorption of the presented MMD in the TM mode is more effective compared to the TE mode, regardless of the incident angle.

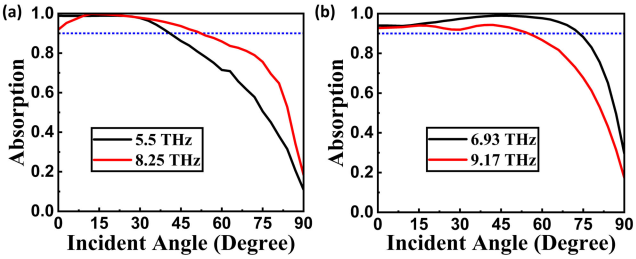

FIGURE 11. Frequency response at different incident angles at(a) TE mode, and (b) TM mode.

Tunability has also been attained in the proposed MMD since the conductivity of VO_2 is temperature dependent. The alteration of conductivity from 200 S/m to 2×10^5 S/m induces a modification in the permittivity of VO_2, thereby leading to a corresponding variation in the reflection and absorption spectra of the MMD and a 96% bandwidth enhancement (4% to 100%) has occurred at the same central frequency as shown in Fig. 12(a)-(b).

Upon observing some key properties of ultra-wideband, polarization-insensitive, and tunable THz MMD, to perform a parametric analysis of the design parameters is essential. For this intent, a systematic study has been conducted in steps: initially, optimization of the dielectric layers, both in terms of thickness and material properties, is accomplished. Later, the dimensions of VO_2 are adjusted. Fig. 13(a)-(b) shows the influence of the thickness of the lower (t_2) and upper dielectric layer (t_3) on the absorption bandwidth. Here, it is apparent that if $t_3 < 4.8$ μm, the bandwidth falls off. On the contrary, if t_2 is greater or below 1.9 μm, the near unity absorption does not persist for the whole spectra. This indicates that the total thickness ($t_3 + t_2$) should be near $\frac{\lambda}{4}$ to agree to impedance matching theory. For the selection of materials, besides PTFE, four different dielectrics (see Table 3) are also chosen on top of polyimide. As shown in Fig. 13(c), obtained bandwidths are 0.77 THz, 3.91 THz, 4.02 THz, 4.57 THz, and 5.68 THz for Si, SiO_2, Polyimide, Topas, and PTFE respectively. Having the lowest dielectric constant compared to other elements,

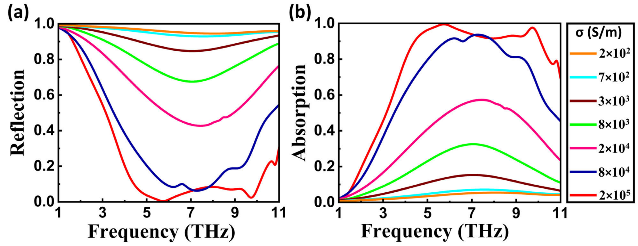

FIGURE 12. (a) The reflection spectrum, and (b) absorption spectrum with different conductivities of VO_2.

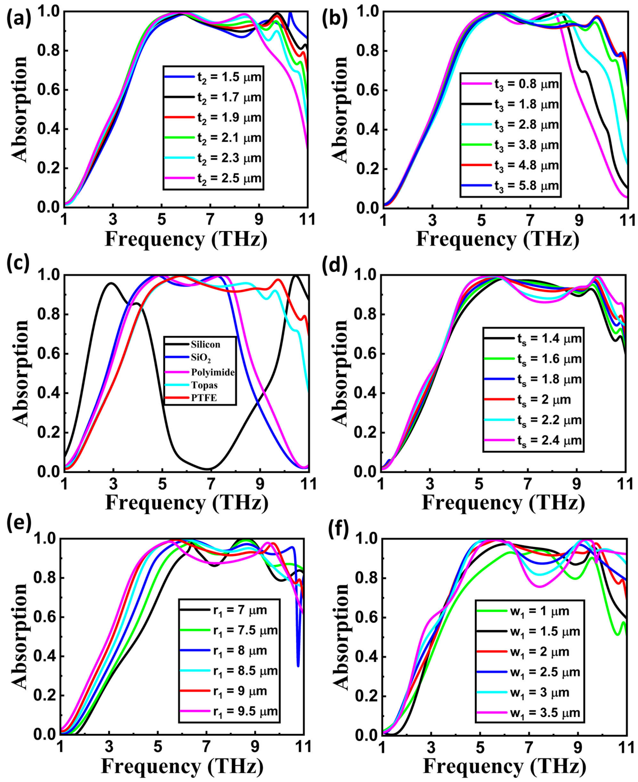

FIGURE 13. The influence of (a) lower dielectric layer thickness t_2, (b) upper dielectric layer thickness t_3, (c) different material in the upper dielectric layer, (d) top resonating surface thickness t_s, (e) ring radius r_1, and (f) ring width w_1.

TABLE 3. Permittivity value of different dielectric materials.

Material	Silicon	SiO_2	Polyimide	Topas
Value	11.7 [46]	3.9	3.5	2.35 [48]

PTFE represents itself as the lightest media and aids in improving absorption for higher bandwidth in subwavelength thickness.

The top pattern of the proposed geometry has been modified in terms of the radius and thickness of the VO_2 rings to access the shift in performance from the optimized state. The study has been accomplished at temperature T = 350 K with the conductivity of VO_2 as 2×10^5 S/m (see, Fig. 13(d)-(f)). Firstly, the middle ring radius (r_1) has been changed, indicating that $r_1 = 9$ μm causes the highest bandwidth with the highest absorption. Though widening the radius enhances the absorber's absorption bandwidth, the overall absorption efficiency degrades due to the change in coupling with the surrounding rings. Next, the slit width (w_1), as equal to the ring width, is adjusted (see, Fig. 13(f)), and it is shown that $w_1 > 2\ \mu$m results in dual bandwidth due to the reduction of the coupling effect in the gap ring. As the slit gap w_1 rises at the concerned spectra, capacitance lowers, and so is the bandwidth. A similar occurrence takes place for $w_1 < 2\ \mu$m due to the rise of parasitic capacitance. Unlike (t_1), the middle ring width (w_2) does not significantly impact the absorber performance. Similar to any microstrip structure, the absorption bandwidth is substantially influenced by the thickness of the VO_2 rings, as shown in Fig. 13(d).

The schematics of the transmission line and equivalent circuit model are provided in Fig. 14(a) and (b). Based on the basics of transmission line theory [49], the input impedance of the dual layer dielectric, Z_{in_D}, can be represented using (12).

$$Z_{in_D} = jZ_D \tan(kt_D) \tag{12}$$

Here, Z_D represents the characteristic impedance of the combined dielectric of total thickness t_D while k indicates the propagation constant. Similarly, the input impedance of the proposed design can be mentioned in (13):

$$Z_{MMD} = \frac{jZ_{VO_2} Z_D \tan(kt_D)}{jZ_D \tan(kt_D) + Z_{VO_2}} \tag{13}$$

where Z_{VO_2} indicates the surface impedance of the VO_2 based top layer. The top VO_2 meta-surface with the periodic ring shapes is modeled as parallel LC circuits with resistors to indicate losses. The capacitance and inductance of the resonator are initially calculated using the standard expression for coupled resonators from [50], and the resulting values are further optimized to achieve the desired output. Here, obtained values are, $L_1 = 1.1963$ pH and $C_1 = 0.432$ fF, $L_3 = 0.54$ pH and $C_3 = 0.957$ fF, $L_5 = 0.51128$ pH and $C_5 = 1.011$ fF, L_7 =0.54 pH and $C_7 = 0.9572$ fF, and $L_9 = 1.1963$ pH and $C_9 = 0.432$ fF. Since the distance among the rings is in the subwavelength range, magnetic coupling and hence coupled inductance becomes prominent [51]. Upon trial and error analysis, the achieved coupled parameters of Fig. 14(b) are set as $L_2 = 1.1963$ pH, $L_4 = 2.271$ pH, $L_6 = 2.271$ pH, $L_8 = 1.892$ pH, $C_2 = 0.273$ fF, $C_4 = 0.2275$ fF, $C_6 = 0.2275$ fF, $C_8 = 0.273$ fF.

The circuit model also incorporates the coupling capacitance C between the top VO_2 meta-surface and the bottom gold layer. The double dielectric layer is represented by the transmission line Z_{in_D}. In comparison to the full wave simulation performed in CST microwave studio, the equivalent circuit of the optimized MMD has been modeled using Keysight Advanced Design System (ADS), and performances have been evaluated in terms of S_{11} (see, Fig. 14(c)) (as provided in (10)). It is evident from Fig. 14(c) that in ideal scenario, with no loss being taken into account in individual LC resonators, the absorption bandwidth is narrower in

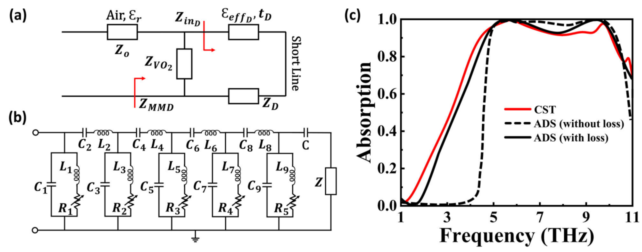

FIGURE 14. (a) Transmission line, (b) equivalent Circuit model of the proposed MMD, and (c) comparison in absorption spectra obtained from CST and ADS.

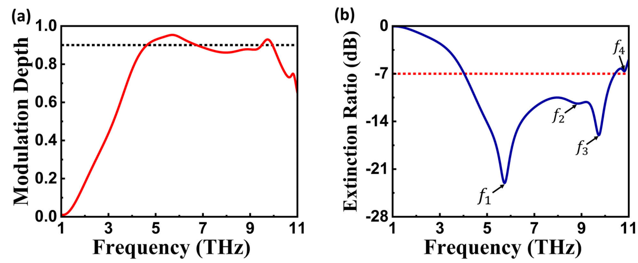

FIGURE 15. (a) Modulation depth (M_d), and (b) Extinction ratio (ER) as a function with frequency.

equivalent circuit model than that in CST. In contrast to full wave simulation scenario, lumped network is taken into account by the equivalent circuit model, which also causes the performance to vary. Upon determining the optimal resistive values, $R_1 = R_5 = 5\Omega$, $R_2 = R_4 = 1.8\Omega$, and $R_3 = 1.5\Omega$, through trial and error procedure, reasonable agreement has been achieved.

To demonstrate the feasibility of our demonstrated design in the state-of-the-art EM light modulators, modulation depth (M_d) and the extinction ratio (ER) are estimated in (14) and (15) [52], [53]:

$$M_d = R_{INS} - R_{MET} = \frac{RP_{MAX} - RP_{MIN}}{P_{INC}} \tag{14}$$

$$ER = -10\log_{10}\frac{RP_{MAX}}{RP_{MIN}} = -10\log_{10}\frac{R_{INS}}{R_{MET}} \tag{15}$$

Here R_{INS} and R_{MET} indicate modulator reflection for VO_2 in insulated and in metallic states, respectively. RP_{MAX}, RP_{MIN} and P_{INC} define the maximum reflected power (VO_2 as insulator), the minimum reflected power (VO_2 as conductor), and the incident power respectively. Practically, the lower and upper threshold values of M_d and ER are 0.9 and -7 dB, respectively [54]. It is evident from Fig. 15(a) that the MD of the designed modulator is above 0.9 From 4.63 to 6.74 THz and 9.5 to 9.94 THz. Similarly, Fig. 15(b) shows the ER of the absorption peaks f_1, f_2, f_3, and f_4 are -23.05 dB, -10.5 dB, -16.01 dB, and -6.63 dB respectively. Hence, it can be concluded that the proposed MMD has huge scope in ultrawideband modulation technology.

Based upon this comprehensive study, a comparison table has been presented in Table 4, flaunting the unique properties of the proposed ultrawideband device as a metamaterial

TABLE 4. Comparison of absorption performance with different VO_2-based wideband absorbers.

Reference	Material	Bandwidth (THz)	Tunable Range	Device Height (μm)
[35]	*Polyimide*	0.28	——	30.6
[55]	SiO_2	0.65	30%-98%	66
[56]	Polyimide	2.77	——	22.3
[57]	SiO_2	3.30	4%-100%	9.4
[58]	Polyimide	3.54	——	9.9
[59]	SiO_2	4.10	3.6%-100%	6.9
[60]	SiO_2	4.66	2%-99%	16.8
This paper	PTFE, Polyimide	5.68	4%-100%	8.9

absorber. Here, all the works achieve tunability due to the presence of temperature dependent VO_2. Such switchable operation can also be accomplished considering photoconductive effect [32], gravity field effect, [33] etc.

IV. CONCLUSION

A systematic design of a dynamically tunable ultra-wideband terahertz metamaterial device, enabling enhanced guided wave propagation, is presented in this work. The presented design showcases a maximum of 5.68 THz bandwidth ranging from 4.42 to 10.10 THz. Incorporating temperature sensitive VO_2 in a symmetrical pattern led to tunability and polarization insensitivity. The Unavailability of experimental resources at the concerned spectrum in the author's country has been greatly compensated by validating the results with equivalent circuit theory. Thanks to its scalable design approach for fabricating multifunctional metamaterial devices, this work makes a significant contribution to the field of ultrathin broadband artificially engineered structures.

REFERENCES

[1] J. Kim, K. Han, and J. W. Hahn, "Selective dual-band metamaterial perfect absorber for infrared stealth technology," *Sci. Rep.*, vol. 7, no. 1, p. 6740, Jul. 2017.

[2] W. Xu, L. Xie, J. Zhu, X. Xu, Z. Ye, C. Wang, Y. Ma, and Y. Ying, "Gold nanoparticle-based terahertz metamaterial sensors: Mechanisms and applications," *ACS Photon.*, vol. 3, no. 12, pp. 2308–2314, Dec. 2016.

[3] Y. I. Abdulkarim, O. Altintas, A. S. Karim, H. N. Awl, F. F. Muhammadsharif, F. Ö. Alkurt, M. Bakir, B. Appasani, M. Karaaslan, and J. Dong, "Highly sensitive dual-band terahertz metamaterial absorber for biomedical applications: Simulation and experiment," *ACS Omega*, vol. 7, no. 42, pp. 38094–38104, Oct. 2022.

[4] R. M. H. Bilal, M. A. Saeed, M. A. Naveed, M. Zubair, M. Q. Mehmood, and Y. Massoud, "Nickel-based high-bandwidth nanostructured metamaterial absorber for visible and infrared spectrum," *Nanomaterials*, vol. 12, no. 19, p. 3356, Sep. 2022.

[5] I. E. Carranza, J. Grant, J. Gough, and D. R. S. Cumming, "Metamaterial-based terahertz imaging," *IEEE Trans. Terahertz Sci. Technol.*, vol. 5, no. 6, pp. 892–901, Nov. 2015.

[6] A. Hossain, M. T. Islam, G. K. Beng, S. B. A. Kashem, M. S. Soliman, N. Misran, and M. E. H. Chowdhury, "Microwave brain imaging system to detect brain tumor using metamaterial loaded stacked antenna array," *Sci. Rep.*, vol. 12, no. 1, p. 16478, Oct. 2022.

[7] J. Canet-Ferrer, *Metamaterials and Metasurfaces*. Norderstedt, Germany: BoD–Books on Demand, 2019.

[8] Y. Zhou, Z. Qin, Z. Liang, D. Meng, H. Xu, D. R. Smith, and Y. Liu, "Ultra-broadband metamaterial absorbers from long to very long infrared regime," *Light, Sci. Appl.*, vol. 10, no. 1, p. 138, Jul. 2021.

[9] Y. I. Abdulkarim, M. Xiao, H. N. Awl, F. F. Muhammadsharif, T. Lang, S. R. Saeed, F. Ö. Alkurt, M. Bakir, M. Karaaslan, and J. Dong, "Simulation and lithographic fabrication of a triple band terahertz metamaterial absorber coated on flexible polyethylene terephthalate substrate," *Opt. Mater. Exp.*, vol. 12, no. 1, pp. 338–359, Jan. 2022.

[10] R. M. H. Bilal, M. A. Baqir, A. Iftikhar, S. A. Naqvi, M. J. Mughal, and M. M. Ali, "Polarization-controllable and angle-insensitive multiband Yagi–Uda-shaped metamaterial absorber in the microwave regime," *Opt. Mater. Exp.*, vol. 12, no. 2, pp. 798–810, Feb. 2022.

[11] S. D. Assimonis and V. Fusco, "Polarization insensitive, wide-angle, ultra-wideband, flexible, resistively loaded, electromagnetic metamaterial absorber using conventional inkjet-printing technology," *Sci. Rep.*, vol. 9, no. 1, p. 12334, Aug. 2019.

[12] M. L. Hakim, T. Alam, M. S. Soliman, N. M. Sahar, M. H. Baharuddin, S. H. A. Almalki, and M. T. Islam, "Polarization insensitive symmetrical structured double negative (DNG) metamaterial absorber for Ku-band sensing applications," *Sci. Rep.*, vol. 12, no. 1, p. 479, Jan. 2022.

[13] M. A. Baqir and P. K. Choudhury, "Hyperbolic metamaterial-based UV absorber," *IEEE Photon. Technol. Lett.*, vol. 29, no. 18, pp. 1548–1551, Sep. 15, 2017.

[14] M. A. Baqir, "Conductive metal–oxide-based tunable, wideband, and wide-angle metamaterial absorbers operating in the near-infrared and short-wavelength infrared regions," *Appl. Opt.*, vol. 59, no. 34, pp. 10912–10919, Dec. 2020.

[15] T. S. Rappaport, Y. Xing, O. Kanhere, S. Ju, A. Madanayake, S. Mandal, A. Alkhateeb, and G. C. Trichopoulos, "Wireless communications and applications above 100 GHz: Opportunities and challenges for 6G and beyond," *IEEE Access*, vol. 7, pp. 78729–78757, 2019.

[16] P. Hillger, J. Grzyb, R. Jain, and U. R. Pfeiffer, "Terahertz imaging and sensing applications with silicon-based technologies," *IEEE Trans. Terahertz Sci. Technol.*, vol. 9, no. 1, pp. 1–19, Jan. 2019.

[17] N. W. Almond, X. Qi, R. Degl'Innocenti, S. J. Kindness, W. Michailow, B. Wei, P. Braeuninger-Weimer, S. Hofmann, P. Dean, D. Indjin, E. H. Linfield, A. G. Davies, A. D. Rakić, H. E. Beere, and D. A. Ritchie, "External cavity terahertz quantum cascade laser with a metamaterial/graphene optoelectronic mirror," *Appl. Phys. Lett.*, vol. 117, no. 4, Jul. 2020, Art. no. 041105.

[18] T. Sun, Z. Bai, Z. Li, Y. Liu, Y. Chen, F. Xiong, L. Chen, Y. Xu, F. Zhang, D. Li, J. Li, W. Zhao, T. Nie, and L. Wen, "Generation of tunable terahertz waves from tailored versatile spintronic meta-antenna arrays," *ACS Appl. Mater. Interfaces*, vol. 15, no. 19, pp. 23888–23898, May 2023.

[19] A. Glück, N. Rothbart, K. Schmalz, and H.-W. Hübers, "SiGe BiCMOS heterodyne receiver frontend for remote sensing with small satellites," *IEEE Trans. Terahertz Sci. Technol.*, vol. 12, no. 6, pp. 603–610, Nov. 2022.

[20] R. M. H. Bilal, M. A. Baqir, P. K. Choudhury, M. M. Ali, and A. A. Rahim, "Tunable and multiple plasmon-induced transparency in a metasurface comprised of silver S-shaped resonator and rectangular strip," *IEEE Photon. J.*, vol. 12, no. 3, pp. 1–13, Jun. 2020.

[21] L. Chen and Z. Song, "Simultaneous realizations of absorber and transparent conducting metal in a single metamaterial," *Opt. Exp.*, vol. 28, no. 5, pp. 6565–6571, Mar. 2020.

[22] C. Chen, M. Chai, M. Jin, and T. He, "Terahertz metamaterial absorbers," *Adv. Mater. Technol.*, vol. 7, no. 5, Dec. 2021, Art. no. 2101171.

[23] B.-X. Wang, Y. He, P. Lou, and W. Xing, "Design of a dual-band terahertz metamaterial absorber using two identical square patches for sensing application," *Nanosc. Adv.*, vol. 2, no. 2, pp. 763–769, 2020.

[24] Y. Wu, S. Tan, Y. Zhao, L. Liang, M. Zhou, and G. Ji, "Broadband multispectral compatible absorbers for radar, infrared and visible stealth application," *Prog. Mater. Sci.*, vol. 135, Jun. 2023, Art. no. 101088.

[25] X. Cheng, R. Huang, J. Xu, and X. Xu, "Broadband terahertz near-perfect absorbers," *ACS Appl. Mater. Interfaces*, vol. 12, no. 29, pp. 33352–33360, Jun. 2020.

[26] W. Pan, X. Yu, J. Zhang, and W. Zeng, "A broadband terahertz metamaterial absorber based on two circular split rings," *IEEE J. Quantum Electron.*, vol. 53, no. 1, pp. 1–6, Feb. 2017.

[27] R.-N. Dao, X.-R. Kong, H.-F. Zhang, and X.-R. Su, "A tunable broadband terahertz metamaterial absorber based on the vanadium dioxide," *Optik*, vol. 180, pp. 619–625, Feb. 2019.

[28] Y. Sun, Y. Shi, X. Liu, J. Song, M. Li, X. Wang, and F. Yang, "A wide-angle and TE/TM polarization-insensitive terahertz metamaterial near-perfect absorber based on a multi-layer plasmonic structure," *Nanosc. Adv.*, vol. 3, no. 14, pp. 4072–4078, 2021.

[29] Y. Wang, D. Zhu, Z. Cui, L. Yue, X. Zhang, L. Hou, K. Zhang, and H. Hu, "Properties and sensing performance of all-dielectric metasurface THz absorbers," *IEEE Trans. Terahertz Sci. Technol.*, vol. 10, no. 6, pp. 599–605, Nov. 2020.

[30] S. Zhou, K. Bi, Q. Li, L. Mei, Y. Niu, W. Fu, S. Han, S. Zhang, J. Mu, L. Tan, W. Geng, and X. Chou, "Patterned graphene-based metamaterials for terahertz wave absorption," *Coatings*, vol. 13, no. 1, p. 59, Dec. 2022.

[31] H. Feng, Z. Xu, K. Li, M. Wang, W. Xie, Q. Luo, B. Chen, W. Kong, and M. Yun, "Tunable polarization-independent and angle-insensitive broadband terahertz absorber with graphene metamaterials," *Opt. Exp.*, vol. 29, no. 5, pp. 7158–7167, Mar. 2021.

[32] S. Liao, J. Sui, and H. Zhang, "Switchable ultra-broadband absorption and polarization conversion metastructure controlled by light," *Opt. Exp.*, vol. 30, no. 19, pp. 34172–34187, Sep. 2022.

[33] J. Qu, H. Pan, Y. Sun, and H. Zhang, "Multitasking device regulated by the gravity field: Broadband anapole-excited absorber and linear polarization converter," *Annalen der Physik*, vol. 534, no. 9, Jul. 2022, Art. no. 2200175.

[34] M. A. Baqir and P. K. Choudhury, "On the VO_2 metasurface-based temperature sensor," *J. Opt. Soc. Amer. B, Opt. Phys.*, vol. 36, no. 8, p. F123, Aug. 2019.

[35] Y. Li, L. Zeng, H. Zhang, D. Zhang, K. Xia, and L. Zhang, "Multifunctional and tunable metastructure based on Vo_2 for polarization conversion and absorption," *Opt. Exp.*, vol. 30, no. 19, pp. 34586–34600, Sep. 2022.

[36] M. J. Akhtar, H. B. Baskey, P. Ghising, and N. M. Krishna, "Microwave effective permittivity of the layered dielectrics and composites using the nonlinear mixing model," *IEEE Trans. Dielectr. Electr. Insul.*, vol. 22, no. 3, pp. 1702–1710, Jun. 2015.

[37] Y. Liu, R. Huang, and Z. Ouyang, "Terahertz absorber with dynamically switchable dual-broadband based on a hybrid metamaterial with vanadium dioxide and graphene," *Opt. Exp.*, vol. 29, no. 13, pp. 20839–20850, Jun. 2021.

[38] N. Mou, B. Tang, J. Li, H. Dong, and L. Zhang, "Switchable ultra-broadband terahertz wave absorption with VO_2-based metasurface," *Sci. Rep.*, vol. 12, no. 1, p. 2501, Feb. 2022.

[39] H. Liu, Z.-H. Wang, L. Li, Y.-X. Fan, and Z.-Y. Tao, "Vanadium dioxide-assisted broadband tunable terahertz metamaterial absorber," *Sci. Rep.*, vol. 9, no. 1, p. 5751, Apr. 2019.

[40] Z. Zheng, Y. Luo, H. Yang, Z. Yi, J. Zhang, Q. Song, W. Yang, C. Liu, X. Wu, and P. Wu, "Thermal tuning of terahertz metamaterial absorber properties based on VO_2," *Phys. Chem. Chem. Phys.*, vol. 24, no. 15, pp. 8846–8853, 2022.

[41] M. Mao, Y. Liang, R. Liang, L. Zhao, N. Xu, J. Guo, F. Wang, H. Meng, H. Liu, and Z. Wei, "Dynamically temperature-voltage controlled multifunctional device based on VO_2 and graphene hybrid metamaterials: Perfect absorber and highly efficient polarization converter," *Nanomaterials*, vol. 9, no. 8, p. 1101, Aug. 2019.

[42] P. U. Jepsen, B. M. Fischer, A. Thoman, H. Helm, J. Y. Suh, R. Lopez, and R. F. Haglund, "Metal-insulator phase transition in a VO_2 thin film observed with terahertz spectroscopy," *Phys. Rev. B, Condens. Matter*, vol. 74, Nov. 2006, Art. no. 205103.

[43] H. Wang, X. Yi, and Y. Li, "Fabrication of VO_2 films with low transition temperature for optical switching applications," *Opt. Commun.*, vol. 256, nos. 4–6, pp. 305–309, Dec. 2005.

[44] L. Liu, L. Kang, T. S. Mayer, and D. H. Werner, "Hybrid metamaterials for electrically triggered multifunctional control," *Nature Commun.*, vol. 7, no. 1, p. 13236, Oct. 2016.

[45] H. Coy, R. Cabrera, N. Sepúlveda, and F. E. Fernández, "Optoelectronic and all-optical multiple memory states in vanadium dioxide," *J. Appl. Phys.*, vol. 108, no. 11, Dec. 2010.

[46] Z. Song and J. Zhang, "Achieving broadband absorption and polarization conversion with a vanadium dioxide metasurface in the same terahertz frequencies," *Opt. Exp.*, vol. 28, no. 8, pp. 12487–12497, Apr. 2020.

[47] H.-T. Chen, "Interference theory of metamaterial perfect absorbers," *Opt. Exp.*, vol. 20, no. 7, pp. 7165–7172, 2012.

[48] P. D. Cunningham, N. N. Valdes, F. A. Vallejo, L. M. Hayden, B. Polishak, X.-H. Zhou, J. Luo, A. K.-Y. Jen, J. C. Williams, and R. J. Twieg, "Broadband terahertz characterization of the refractive index and absorption of some important polymeric and organic electro-optic materials," *J. Appl. Phys.*, vol. 109, no. 4, Feb. 2011, Art. no. 043505.

[49] H. R. Taghvaee, H. Nasari, and M. S. Abrishamian, "Circuit modeling of graphene absorber in terahertz band," *Opt. Commun.*, vol. 383, pp. 11–16, Jan. 2017.

[50] S. Bhattacharyya, S. Ghosh, and K. V. Srivastava, "Equivalent circuit model of an ultra-thin polarization-independent triple band metamaterial absorber," *AIP Adv.*, vol. 4, no. 9, Sep. 2014, Art. no. 097127.

[51] J.-S. Hong, *Microstrip Filters for RF/Microwave Applications*, 2nd ed. Hoboken, NJ, USA: Wiley, Mar. 2011.

[52] Y. Li, W. Gao, L. Guo, Z. Chen, C. Li, H. Zhang, J. Jiao, and B. An, "Tunable ultra-broadband terahertz perfect absorber based on vanadium oxide metamaterial," *Opt. Exp.*, vol. 29, no. 25, pp. 41222–41233, Dec. 2021.

[53] S. G.-C. Carrillo, G. R. Nash, H. Hayat, M. J. Cryan, M. Klemm, H. Bhaskaran, and C. D. Wright, "Design of practicable phase-change metadevices for near-infrared absorber and modulator applications," *Opt. Exp.*, vol. 24, no. 12, pp. 13563–13573, Jun. 2016.

[54] E.-T. Hu, T. Gu, S. Guo, K.-Y. Zang, H.-T. Tu, K.-H. Yu, W. Wei, Y.-X. Zheng, S.-Y. Wang, R.-J. Zhang, Y.-P. Lee, and L.-Y. Chen, "Tunable broadband near-infrared absorber based on ultrathin phase-change material," *Opt. Commun.*, vol. 403, pp. 166–169, Nov. 2017.

[55] S. Wang, C. Cai, M. You, F. Liu, M. Wu, S. Li, H. Bao, L. Kang, and D. H. Werner, "Vanadium dioxide based broadband THZ metamaterial absorbers with high tunability: Simulation study," *Opt. Exp.*, vol. 27, no. 14, pp. 19436–19447, 2019.

[56] Y. Qiu, D.-X. Yan, Q.-Y. Feng, X.-J. Li, L. Zhang, G.-H. Qiu, and J.-N. Li, "Vanadium dioxide-assisted switchable multifunctional metamaterial structure," *Opt. Exp.*, vol. 30, no. 15, pp. 26544–26556, Jul. 2022.

[57] G. Z. Wu, X. F. Jiao, Y. D. Wang, Z. P. Zhao, Y. B. Wang, and J. G. Liu, "Ultra-wideband tunable metamaterial perfect absorber based on vanadium dioxide," *Opt. Exp.*, vol. 29, pp. 2703–2711, Jan. 2021.

[58] Y. Dong, D. Yu, G. Li, M. Lin, and L.-A. Bian, "Terahertz metamaterial modulator based on phase change material VO_2," *Symmetry*, vol. 13, no. 11, p. 2230, Nov. 2021.

[59] R. Zhang, Y. Luo, J. Xu, H. Wang, H. Han, D. Hu, Q. Zhu, and Y. Zhang, "Structured vanadium dioxide metamaterial for tunable broadband terahertz absorption," *Opt. Exp.*, vol. 29, no. 26, pp. 42989–42998, Dec. 2021.

[60] Y. Chen and J.-S. Li, "Switchable dual-band and ultra-wideband terahertz wave absorber," *Opt. Mater. Exp.*, vol. 11, no. 7, pp. 2197–2205, Jul. 2021.

S. M. RAKIBUL HASAN SHAWON (Student Member, IEEE) received the B.Sc. degree in electrical and electronic engineering with a major in communication from the University of Dhaka, Bangladesh, in 2021, where he is currently pursuing the M.Sc. degree in electrical and electronic engineering with a major in communication and signal processing. His research interests include nanoscale electronic and optoelectronic devices with meta-surface geometry, SPR-based nanosensors for biosensing applications, tunable metamaterial devices operating in THz and GHz frequencies, and genetic algorithm-based plasmonic RI sensors.

SAJIB KAPALI received the B.Sc. degree in electrical and electronic engineering, majoring in computer and communication, from the University of Dhaka, Bangladesh, in 2020. His research focuses on various areas within the field of electromagnetics, such as applied electromagnetics, reconfigurable RF/millimeter wave circuits, and metamaterial devices. In addition, he is particularly interested in utilizing generative adversarial networks (GANs) to design metasurfaces.

IMI BINTEY FARIHA RAHMAN (Student Member, IEEE) received the B.Sc. degree in electrical and electronic engineering, majoring in communication from the University of Dhaka, Bangladesh, in 2021, where she is currently pursuing the M.Sc. degree with a major in communication and signal processing. Her research interests include tunable metamaterial absorbers, plasmonic refractive index (RI) sensors, and subwavelength thick devices.

SHARNALI ISLAM received the Ph.D. degree from the University of Illinois at Urbana–Champaign, Champaign, IL, USA, in 2014. She joined the University of Dhaka, in 2017, where she is currently an Assistant Professor of electrical and electronic engineering. Before her career in academia, she was a Device Engineer with Intel Company, USA, working in the NAND Memory Cell Group, defining requirements and roadmap for NAND cell parameters towards meeting the overall technology goal. She was the Faculty Group Advisor of the IEEE WIE Student Branch Dhaka University, from 2018 to 2019. She has coauthored a book chapter and a total of 27 journal publications in highly reputed international journals. Her research interests include photonic devices, electrical and thermal modeling of nano-scale computational and energy harvesting devices, and VLSI technology.

KHALEDA ALI received the M.S. degree from the University of Dhaka, Bangladesh, in 2008, and the Ph.D. degree from the Department of Electronic Engineering, Queen Mary University of London. She is currently an Assistant Professor with the Department of Electrical and Electronic Engineering, University of Dhaka. Her research interests include wireless channel modeling at millimeter wave and terahertz frequencies energy harvesting and computational electro-magnetics.